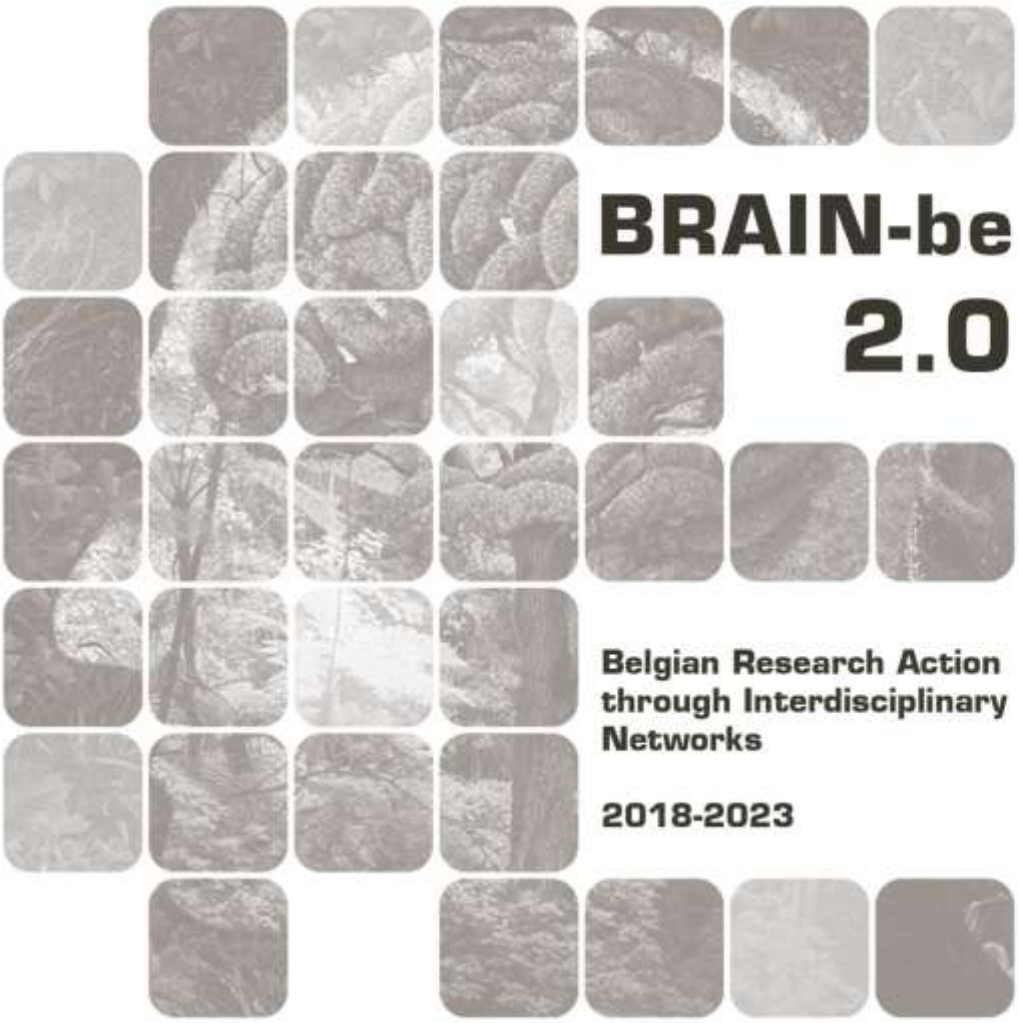

MOMENTUM

MesOscale Modelling for ExoMars TGO/NOMAD To Understand gravity waves in the Martian atmosphere

Dr. Lori Neary (BIRA-IASB) – Dr. Loïc Trompet (BIRA-IASB) – Dr. Frank Daerden (BIRA-IASB) – Dr. Justin T. Erwin (BIRA-IASB)

Pillar 1: Challenges and knowledge of the living and non-living world

belspo .be

NETWORK PROJECT

MOMENTUM

MesOscale Modelling for ExoMars TGO/NOMAD To Understand gravity waves in the Martian atmosphere

Contract - B2/223/P1/MOMENTUM

FINAL REPORT

PROMOTORS: Dr. Lori Neary (Royal Belgian Institute for Space Aeronomy)

AUTHORS: Dr. Lori Neary (Royal Belgian Institute for Space Aeronomy),
Dr. Loïc Trompet (Royal Belgian Institute for Space Aeronomy),
Dr. Frank Daerden (Royal Belgian Institute for Space Aeronomy),
Dr. Justin T. Erwin (Royal Belgian Institute for Space Aeronomy)

Published in 2025 by the Belgian Science Policy Office
WTCIII
Simon Bolivarlaan 30 bus 7
Boulevard Simon Bolivar 30 bte 7
B-1000 Brussels
Belgium
Tel: +32 (0)2 238 34 11
http://www.belspo.be
http://www.belspo.be/brain-be

Contact person: Koen Lefever
Tel: +32 (0)2 238 35 51

Neary, L., Trompet, L. Daerden, F. Erwin, J.T., ***MesOscale Modelling for ExoMars TGO/NOMAD To Understand gravity waves in the Martian atmosphere***. Final Report. Brussels: Belgian Science Policy Office 2025 – 35 p. (BRAIN-be 2.0 - (Belgian Research Action through Interdisciplinary Networks))

TABLE OF CONTENTS

ABSTRACT

Context

Studying the present Martian climate provides insights into both its past atmospheric evolution and broader planetary processes. Observations and climate models are closely interlinked: models aid data retrieval, while observations constrain and validate simulations. Discrepancies between the two can identify missing or poorly represented processes. Since observations are often limited in space and time, models fill critical gaps, requiring accurate representation of known atmospheric features. Model resolution, constrained by computational power, limits the explicit treatment of small-scale dynamics, which must be parameterised. Among these, gravity waves—generated by topography or weather systems—play a key role in transferring energy and momentum to the upper atmosphere. Despite their relatively small spatial scale, they exert significant thermal and dynamical forcing, making their inclusion in Martian climate models essential for accurate simulation of the planet's atmospheric system.

Objectives

The goal of the MOMENTUM project is to gain a better understanding of the impact of gravity waves on large scale circulation and to improve Global Climate Models (GCMs) to more accurately represent these effects in climate simulations. By using observations from the Nadir and Occultation for MArs Discovery (NOMAD) instrument onboard the ExoMars Trace Gas Orbiter (TGO), we can look for signatures of gravity waves and attempt to quantify their potential effects on the mean flow. These observed effects can then be compared to those calculated in the GCM by the gravity wave drag (GWD) parameterisations, which are not well constrained. There are several parameters that can be adjusted in these schemes, and with the observations, we can work towards a more realistic simulation. The direct effect of gravity waves on the simulated wind fields can modify the overall global circulation and have secondary effects on the thermal structure in the upper atmosphere. The region where waves are thought to break is a key transition zone between the upper and lower atmosphere, so this is an important process to represent well in a GCM.

Conclusions

We see gravity waves frequently in the TGO/NOMAD observations and are building a climatology of activity over several Martian years. We see some differences in sunrise and sunset behaviour, particularly in the southern hemisphere winter.

By analysing the temperatures and wave activity observed by NOMAD, we have been able to tune the GEM-Mars GCM parameterisations of gravity wave drag to better match the observations and provide more realistic simulations.

This project has enabled us to have high-resolution simulations of the Martian atmosphere, and more simulations are planned to understand better the seasonal and diurnal differences in wave activity.

We have found several examples of cold pockets likely due to wave activity where there is potential for the formation of CO_2 ice clouds. This provides the opportunity to study this further and improve the model implementation of these types of clouds.

This project has also allowed for other improvements to the model, such as the implementation of a better formulation for the radiative transfer in non-local thermodynamic equilibrium conditions.

Keywords

Mars atmosphere, gravity waves, Global Climate Modelling, parameterisations

1. INTRODUCTION

Through the study of the current climate on Mars, we can gain some insight into its past and how planetary atmospheres evolve over time. Observational data and modelling work together to help paint a picture of the processes occurring in the atmosphere. There are synergies and feedback between the two disciplines, we use model simulations as inputs, or a priori, to the data retrieval process and the retrieved data are used to help evaluate the model performance. By comparing simulations with observations, we can determine how well we understand the processes occurring in the atmosphere. If there is a time or location where the model results do not match well with the observations, we can try to determine what process is missing or not well represented in the model. Observations of the atmosphere can reveal a great deal but there are often limits to their coverage in space and time, so we use atmospheric models to help close those gaps and provide a clearer interpretation of what is observed. Therefore, it is crucial that we fully represent the features known in the atmosphere to have the most accurate representation in our simulations. The model resolution (how the planetary grid is divided in the horizontal and vertical) is an important factor in how accurate the simulation is, and this is often driven by the available computational power. Long-term simulations for climate (timescale of years) tend to have a resolution that is on the order of hundreds of kilometres, so small-scale processes like convection, eddies and waves must be parameterised (using a simplified process to represent their effect on the large-scale). Gravity waves are one of those processes that take place on a scale smaller than most global climate model grids. They are formed when air is stably stratified and are triggered by wind flow over topography (orographic) or by weather events such as frontal systems, jet streams and convection (non-orographic). As the resulting wave propagates upward where the atmosphere is less dense, the amplitude grows, and energy and momentum are transferred from the lower to the upper atmosphere. While the waves are relatively small, ranging in wavelength from tens to hundreds of kilometres, they have a large impact through thermal and dynamical forcing on the climate and therefore need to be accounted for in atmospheric climate models.

2. STATE OF THE ART AND OBJECTIVES

On Mars, gravity-wave induced density and temperature fluctuations have been observed by orbiting platforms (e.g., England et al., 2017; Vals et al., 2019; Heavens et al., 2020; Starichenko et al., 2021;2024), during aerobraking (Creasey et al., 2006; Fritts et al., 2006) and from the surface (Guzewich et al., 2021). Their effects are also seen in airglow imagery (Altieri et al., 2012). Gravity waves are thought to be one of the main sources of cold pockets in the upper atmosphere of Mars, allowing for the condensation of its main constituent, CO_2, and the formation of CO_2 ice clouds (Määttänen et al., 2010; González-Galindo et al., 2011; Spiga et al., 2012; Yiğit et al., 2015; Liuzzi et al., 2021). Recent observations led to speculation on their role in the formation of water ice clouds as well (Clancy et al., 2021). Yiğit et al. (2021) stressed the importance of gravity waves in linking the lower to upper atmosphere in terms of mechanisms for the escape of hydrogen in the Martian atmosphere. As a result of observations from NASA's MAVEN mission, ESA's Mars Express and ExoMars TGO, the topic of high-altitude water vapour and hydrogen escape received much attention (Chaffin et al., 2017; Stone et al., 2020; Villanueva et al., 2021; Neary et al., 2020; Daerden et al., 2022). There is a need for a better understanding of the role that gravity waves play in the mechanisms responsible for hydrogen escape.

As mentioned above, the impact of these waves must be simplified or parameterised in global models to have a more accurate simulation of the temperature and circulation of the atmosphere. There are several parameterisations for gravity waves, often from terrestrial models, but none are very well constrained (see Medvedev and Yiğit (2019) for an overview). Apart from one scheme (Yiğit et al., 2008), most models use two parameterisations, one for orographically induced waves (e.g., Lindzen et al., 1981; Palmer et al., 1986; McFarlane et al., 1987), and another for non- orographic sources such as wind shears, convection and other weather phenomena (e.g., Hines, 1997a;b; Lott et al., 2012; Lott and Guez et al., 2013; Gilli et al., 2020). As computing power increases, efforts and advances have been made on this subject using higher resolution global models (Kuroda et al., 2015;2020). These simulations had a horizontal resolution of approximately 67 km x 67 km and therefore resolved a larger spectrum of wavelengths. This work provided some insight into gravity wave sources and behaviour but there is still some effort required to translate the results into better parameterisations. Limited area mesoscale models (covering a sub-set of the globe) have also been used to investigate gravity waves and their role in the formation of CO_2 ice clouds (Spiga et al., 2012), to compare with lander data (Guzewich et al., 2021) and to investigate gravity waves as seen in airglow observations (Altieri et al., 2012). Listowski et al. (2014) continued the work of Spiga et al. (2012) by applying a one-dimensional CO_2 cloud microphysics model to the output from the idealised mesoscale simulations and Mathé et al. (2021) incorporated the scheme into a GCM. These studies have laid a solid foundation for the MOMENTUM project to build on.

3. METHODOLOGY

In the following sections we will describe the tools and methods used for this project. First, we describe the NOMAD instrument and observations used followed by a brief overview of the GEM-Mars GCM. The methodology for the analysis of gravity waves and tuning of the model will be given.

TGO/NOMAD observations

NOMAD began science operations in April 2018, just before a large planet-encircling dust storm in Mars Year (MY) 34 and has been taking measurements now for more than 3.5 Martian years.

The instrument is comprised of a suite of spectrometers capable of observing from the ultraviolet-visible to the infrared wavelength range (Neefs et al., 2015). The instrument observes the atmosphere in several geometries: nadir, limb and solar occultation. For this project, we use profiles measured in solar occultation (SO) mode in the infrared wavelength range. This observing mode consists of keeping the instrument line of sight (LoS) pointing to the Sun and observing the atmosphere in altitude slices as the sun rises or sets. This gives high vertical resolution (<2 km on average) profiles at the terminator region. The SO channel of NOMAD is a diffraction grating spectrometer with an Acousto-Optical Tunable Filter (AOTF) which allows for the selection of narrow spectral windows of ~ 20-30 cm^{-1} (referred to as diffraction orders). For this work, we look at the observations taken with diffraction orders 132, 148 and 165. Table 1 gives the starting and ending wavenumber of the diffraction orders used for this study. With these spectral windows, carbon dioxide (CO_2) gas density can be retrieved, with sensitivity at different altitudes. In the future, we will add retrievals from order 156 to fill the gap between 100-130 km.

Table 1 NOMAD diffraction orders used in this study

Diffraction order	Starting wavenumber (cm^{-1})	Ending wavenumber (cm^{-1})	Altitude range of measurements
132	2966.49	2990.14	< 60 km
148	3326.07	3352.58	60-100 km
165	3708.11	3737.67	> 130 km

From the retrieved CO_2 density, we can infer a temperature using the hydrostatic equilibrium equation. The method is explained fully in Trompet et al. (2023a).

The GEM-Mars GCM

The GEM-Mars three-dimensional general circulation model takes advantage of the cutting-edge efforts made by the numerical weather prediction (NWP) community by using the operational framework and dynamical core of the Global Environmental Multiscale (GEM) model from the Recherche en Prévision Numérique (RPN) division of Environment Canada (Côté et al., 1998a, 1998b; Yeh et al., 2002). We use version 4.2.0 of GEM, which has been converted from the terrestrial application for the simulation of the Mars atmosphere. The GEM-Mars model describes the meteorology, circulation, dust, clouds, water, polar caps, radiation and atmospheric chemistry from the surface up to 150 km altitude. The model is typically run at a horizontal resolution of 4°x4°, which is approximately 237 km x 237 km at the equator.

GEM includes a parameterization for gravity wave generation by airflow over topography in the physics package for the Earth (McFarlane, 1987) as well as a low-level orographic blocking scheme

(Zadra et al., 2003) based on that of Lott and Miller (1997). The sub-grid scale parameters are derived from the high-resolution MOLA topography. The gravity wave drag (GWD) scheme relies on the saturation concept of Lindzen (1981), which describes the effects of wave breaking associated with the onset of convective instability. The changes in the horizontal wind due to GWD depend on the subgrid scale orographic variance, the atmospheric stratification, local density height scale and a tunable parameter defined as the product of a representative value of horizontal wavenumber and an efficiency factor less than one.

The tendency of orographic GWD on the horizontal wind **V** is:

$$\left(\frac{\partial \boldsymbol{V}}{\partial t}\right)_{GWD} = -\boldsymbol{n}\frac{\partial}{\partial \sigma}(MU) \tag{1}$$

where **n** is a unit vector parallel to the mean flow at a reference σ level near the surface, U = **n** · **V** is the local wind component parallel to that at the reference level. M is defined as:

$$M = h_e^2 \frac{E\mu_e}{2}\sigma\frac{NA^2}{H} \tag{2}$$

where H is the local density height scale, N is the Brunt-Väisälä frequency, E is an efficiency factor less than unity, μ_e and h_e are the horizontal wavenumber and amplitude for a typical wave. The quantity $E\mu_e/2$ is regarded as a tunable parameter.

The wave amplitude, A, is such that the wave momentum flux, MU, is independent of σ except in wave saturation regions where A is chosen so that:

$$\frac{AN}{F_c U} = 1 \tag{3}$$

where F_c is a critical value of the local inverse Froude number.

For non-orographically sourced waves, we use the terrestrial GEM parameterisation from Hines (1997a;b). The scheme employs Doppler-spread theory, wherein a continuous spectrum of gravity wave phase speeds interacts with the evolving background wind field. As the waves propagate upward through the stably stratified and progressively rarified Martian atmosphere, their amplitudes increase until nonlinear effects induce saturation and dissipation, leading to a gradual deposition of momentum and energy. This process is highly dependent on the Doppler shifting of the wave spectrum, which selectively filters waves according to their intrinsic phase speed relative to the ambient flow. By distributing drag over a broad altitude range rather than at discrete breaking levels, the scheme attempts to capture the cumulative dynamical forcing of non-orographic gravity waves.

The scheme launches a continuous spectrum of gravity waves at a prescribed source level representing unresolved tropospheric sources such as convection and fronts. Each spectral component is characterised by a vertical wavenumber, with the launch spectrum bounded below by a minimum wavenumber corresponding to a prescribed vertical wavelength. To prevent unrealistically strong contributions from long vertical waves, the power spectral density for wavenumbers below this cutoff is given a positive slope, ensuring increasing variance with increasing vertical wavenumber up to the cutoff.

As the spectrum propagates upward through the background wind and stratification, Doppler shifting continuously redistributes wave power across phase speeds and vertical wavenumbers. A variable upper cutoff in vertical wavenumber, increasing with altitude, acts as a dissipation threshold: any spectral element Doppler-spread beyond this limit is considered saturated and deposits its momentum locally. In this way, the scheme translates nonlinear filtering and instability (both convective and shear) into a smoothly distributed vertical divergence of momentum flux.

Tuning of GWD schemes for low resolution

For the orographic gravity wave scheme, the quantity $E\mu_e/2$ in Equation 2 was modified from 8.e-6 to 5.e-6 after sensitivity tests. As μ_e represents the horizontal wavenumber, this would imply a higher horizontal wavelength than the value used for terrestrial application.

For the non-orographic scheme, there are several tunable parameters, such as the level at which waves are expected to be launched and the lower bound vertical wavenumber, which limits the maximum vertical wavelength of the spectrum allowed (see Hines, 1997; 2004; Charron et al., 2002). We modified the launching level to be appropriate for Mars and modified the horizontal wavenumber to 5.e-6. We also increased the altitude at which the effects taper off exponentially.

Simulations and analysis

We performed simulations at 4°x4° for MY 34-37 to compare with NOMAD observations. The model timestep is ~ 30 minutes and we save the output at every timestep and then extract model profiles at the same time and location of the occultations and interpolate onto the same grid for comparison. We look at individual profiles as well as seasonal and zonal averages.

We also performed a preliminary model simulation at a horizontal resolution of 1°x1° to see how the model resolves waves, as shown in Figure 1.

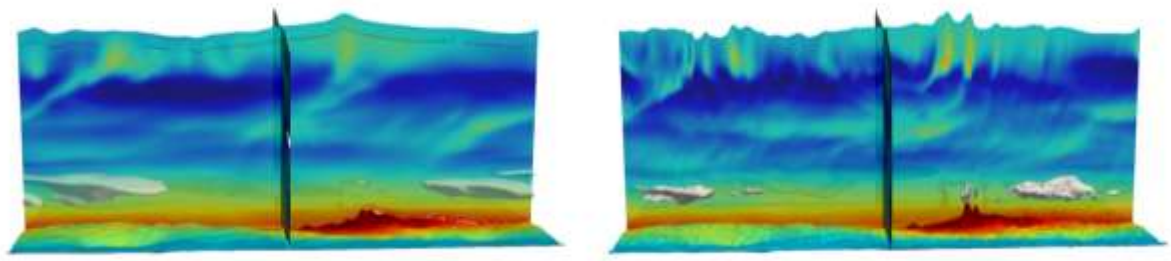

Figure 1 Snapshots of model simulations at 4x4 (left) and 1x1 (right). The coloured contours are temperature slices and white isosurfaces represent water ice clouds. More structure in the temperature field can be seen in high resolution simulation.

With the individual temperature profiles from NOMAD and the GCM, we fit a polynomial to obtain a background or average profile ($\overline{T}$). We experimented with different orders of polynomial and present here results using a 6^{th} order polynomial. By subtracting the background from the actual temperature ($T'=T-\overline{T}$), we have a picture of the perturbations in the atmosphere.

In addition to these perturbations, we can look at the potential energy and the Brunt-Väisälä frequency (N^2) which characterises the convective stability in the atmosphere, given in Equation 5:

$$N^2 = \frac{g}{T}\left(\frac{dT}{dz} + \frac{g}{c_p}\right) \quad (5)$$

Where g is the acceleration due to gravity and c_p is the specific heat capacity at constant pressure. When $N^2 > 0$, the atmosphere is stably stratified and when $N^2 < 0$ the atmosphere is unstable and no longer supports wave propagation. This means that when N^2 is close to 0 or just negative, we can have strong dissipation of waves. The potential energy (quantifying stored buoyancy energy) is given by Equation 6:

$$E_p = \frac{1}{2}\left(\frac{g}{N}\right)^2 \left(\frac{|T'|}{\bar{T}}\right)^2 \quad (6)$$

A large E_p implies strong vertical displacements and temperature perturbations and reflects how much energy it requires (in terms of buoyancy) to hold air parcels away from equilibrium.

Using Fourier decomposition, we then estimate the vertical flux of horizontal momentum per unit mass using Equation 7:

$$F = \sum_{k,m} \frac{1}{2}\frac{k_h}{m}\left(\frac{g}{N}\right)^2 \left(\frac{|T'_{k,m}|}{\bar{T}}\right)^2 \quad (7)$$

where k_h and m are the horizontal and vertical wavenumbers and $|T'_{k,m}|$ is the amplitude of the harmonic's perturbation. We use a horizontal wavelength ($\lambda_h = 2\pi/k_h$) of 300 km.

We then compute momentum lost by a breaking harmonic (gravity wave drag or GWD) to compare with GCM calculated GWD from parameterisations using Equation 8.

$$GWD = \frac{1}{\bar{\rho}}\frac{d\bar{\rho}F}{dz} \quad (8)$$

This analysis method is further described in Starichenko et al., 2024.

4. SCIENTIFIC RESULTS AND RECOMMENDATIONS

Temperature comparisons

We first compare the retrieved temperatures from NOMAD with simulated values from GEM-Mars. This was first done in Trompet et al. (2023b) and is shown in Figure 2. Averaged profiles like this provide an initial metric to show the performance of the GCM but lose the information regarding small scale waves, which can be seen in the NOMAD profiles shown in Figure 3, as an example. One aspect that is observed in the NOMAD dataset is the presence of tides, which can play a role in the dissipation of gravity waves (some examples are shown in Figures 6 and 7 of Trompet et al., 2023b). The sparsity of the data points makes it difficult to make firm conclusions so the use of the GCM is very valuable. Figure 4 is a snapshot of an animation showing the full picture of the atmosphere using the data from the GEM-Mars GCM. The top frame is a vertical slice with longitude on the x-axis and height on the y-axis at a latitude around 62ºS. The bottom frame is the horizontal slice at 70 km. Using this kind of visualization, we can get a better picture of the simulated temperature structures and how tides behave.

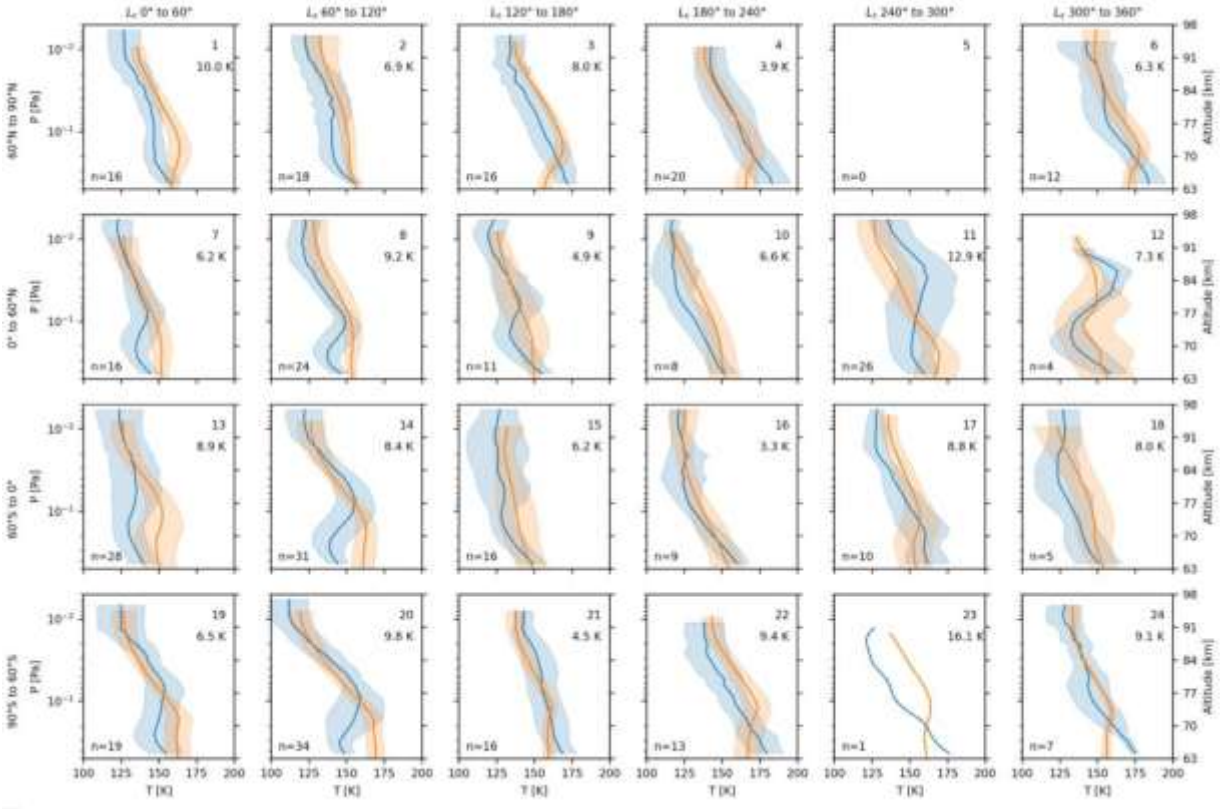

Figure 2 Comparison of GEM-Mars (orange) and NOMAD (blue) averaged temperature profiles for different seasons and latitude bands. The profiles here are for the morning terminator (from Trompet et al., 2023b)

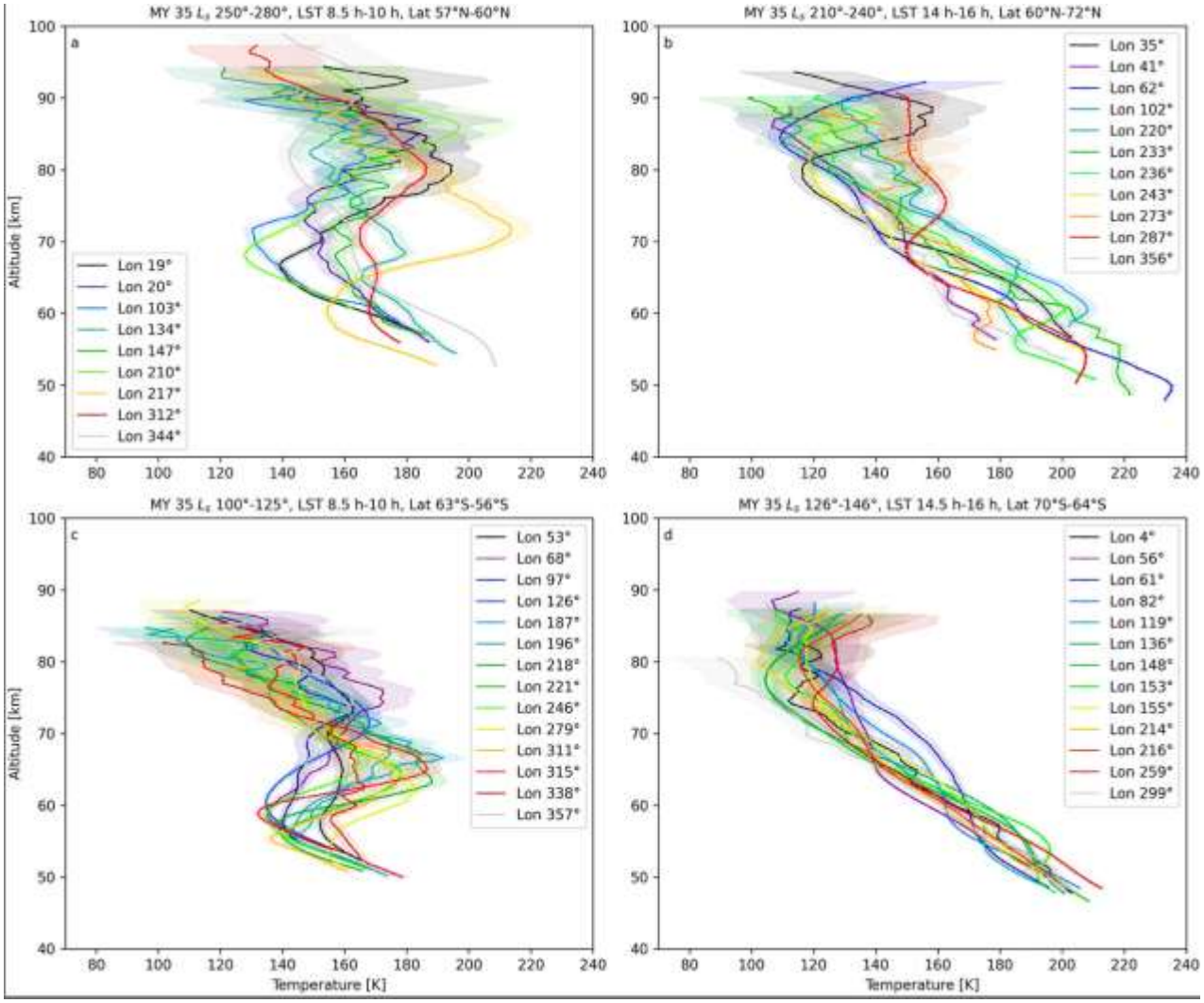

Figure 3 Individual NOMAD profiles showing the amount of structure and the presence of waves (from Trompet et al., 2023b)

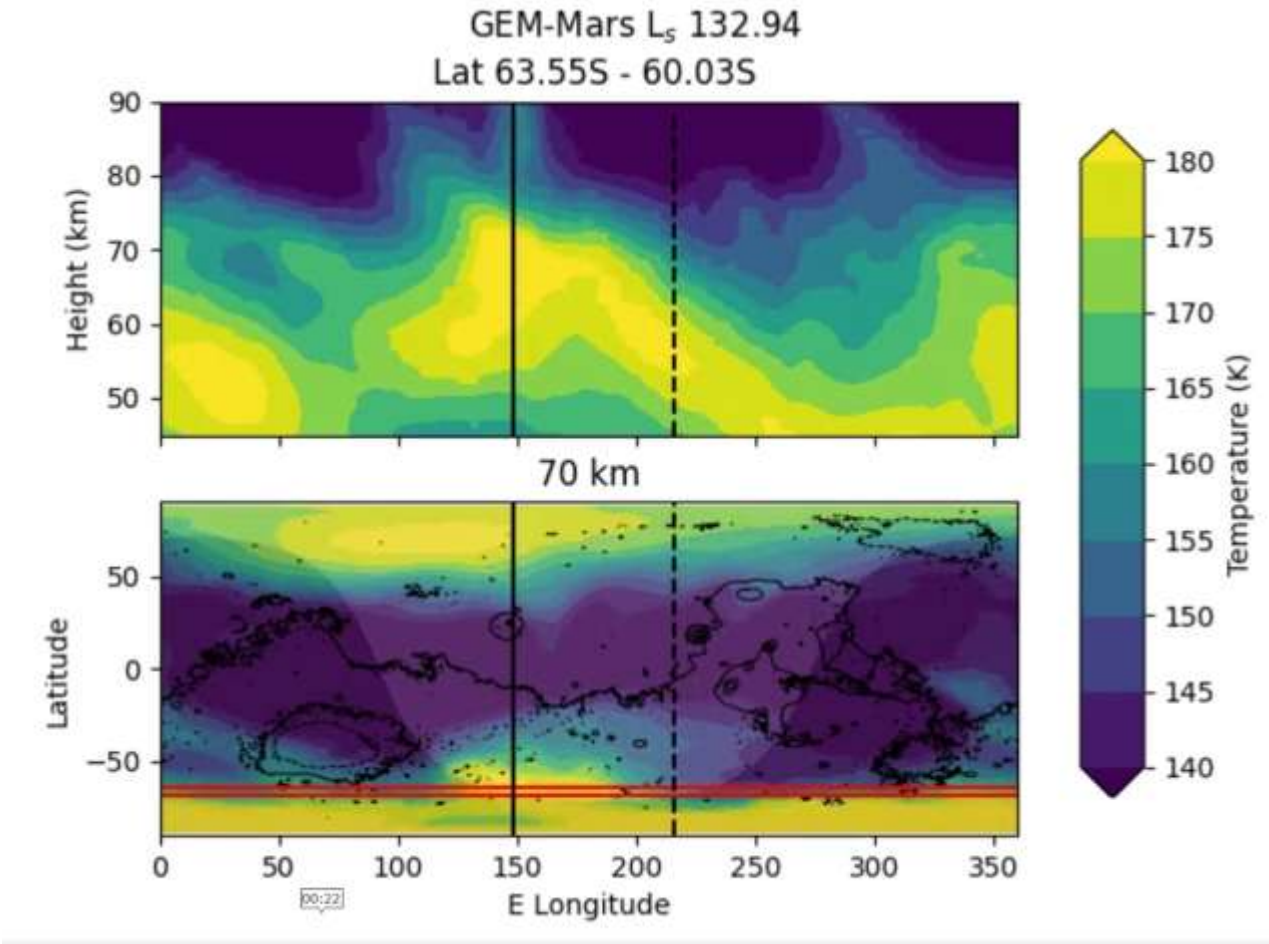

Figure 4 Snapshot from an animation of a GEM-Mars simulation showing a vertical slice in the atmosphere at around 62ºS, the location of a NOMAD occultation (top frame). The bottom frame is the horizonal slice at 70 km. The shaded area is night-time and the solid and dashed lines indicate the longitude where the terminator crosses the latitude of interest (where NOMAD observed).

During the project, the TGO/NOMAD solar occultation data was reprocessed and new comparisons to GEM-Mars simulations of temperature were performed. The reprocessed data has a stricter cut-off in the case of saturation of the CO_2 absorption lines, eliminating potentially inaccurate retrievals at the lower bounds of the profiles (around 40-60 km). We have also compared the modelled temperatures with 2 other TGO instruments, the Atmospheric Chemistry Suite (ACS) Mid InfraRed (MIR) and Near InfraRed (NIR) instruments (Korablev et al., 2018; Belyaev et al., 2022). The ACS data was kindly provided through our participation in an International Space Science Institute (ISSI) project. Figure 5 shows the differences in temperature between model and observations at 80 km, a region where gravity wave (GW) breaking often occurs. This is also the region where we see the largest differences in modelled and observed temperatures. The data presented is for the last half of MY34 (which includes a large planet-encircling dust storm), MY35 and MY36 (for NOMAD). There should be little direct effect from aerosols at this altitude, except in the case of the MY34 dust storm which occurred around solar longitude (L_s) of 195-220°, where dust was lofted up to higher altitudes.

The model tends to over-predict temperatures at this altitude and on average, it is more than 20 K too high around 23% of the time. At 60 km, the differences are smaller, over-predicting by 20 K around 9.5% of the time on average. Table 1 provides a summary of the percentage of observations where GEM-Mars over-predicts by more than 20 K at altitudes of 60, 70 and 80km. At northern latitudes (See

Figure 5 upper panel), MY35 and MY36 behave similarly, with an over-prediction in the model in the first half of the year and an underprediction during the dusty season around L_s=620° and 980°, close to northern hemisphere winter solstice. At the southern latitudes, there is a model underprediction right at the time of the global dust storm, indicating that we may not be lofting sufficient dust to higher altitudes to provide more realistic temperatures.

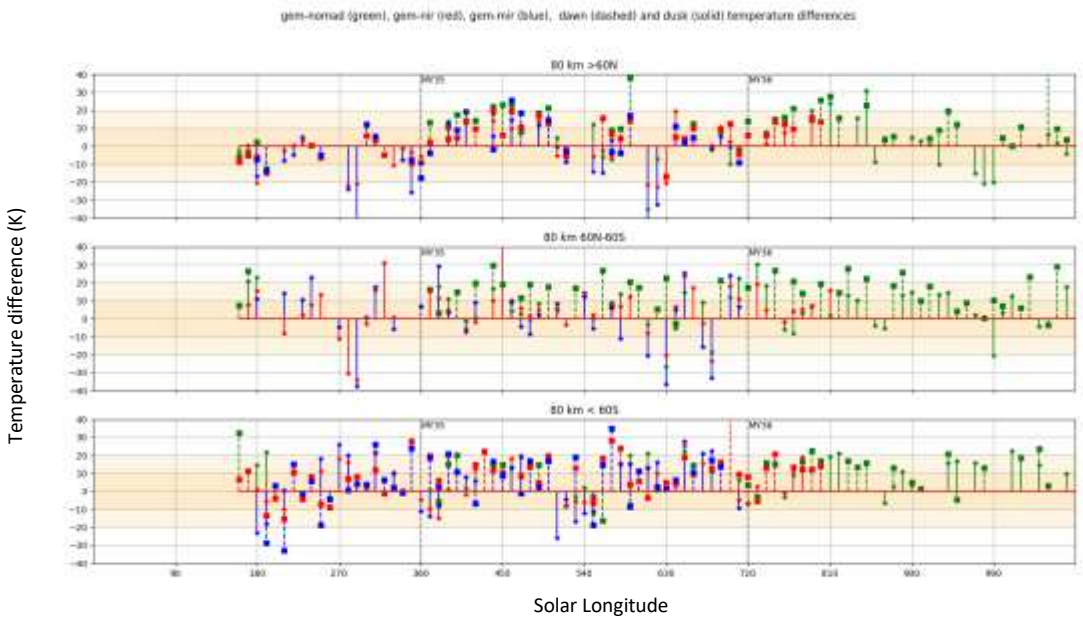

Figure 5 Temperature differences between GEM-Mars and NOMAD (green), ACS-MIR (red) and ACS-NIR (blue), averaged in bins of 10º of solar longitude. Positive values indicate that GEM-Mars is warmer than observations. The stars with solid lines are sunset occultations and the dashed lines with squares are sunrise occultations. The top figure is for observations north of 60˚N, the centre is for 60˚N-60˚S and the bottom figure is for south of 60˚S. The darker shaded regions are +/- 10 K and lighter regions are +/- 20 K for reference.

Table 2 Summary of percentages where GEM-Mars over-predicts temperature by more than 20K

North > 60°N	**% where GEM-Mars temperatures > 20K higher than NOMAD for sunrise occultations**	**% where GEM-Mars temperatures > 20K higher than NOMAD for sunset occultations**
80 km	23.7	11.4
70 km	23.2	20.7
60 km	6.0	9.5
Equatorial 60°S – 60°N		
80 km	38.2	17.9
70 km	23.9	17.9
60 km	10.3	12.4
South < 60°S		
80 km	26.6	22.7
70 km	30.3	15.2
60 km	12.2	6.8

In Figure 6, we show the full dataset latitude-longitude distribution of the ACS-NIR observations (left) and model values (right) at 80km. The model overprediction can be seen at most latitudes but is slightly more pronounced in the polar regions.

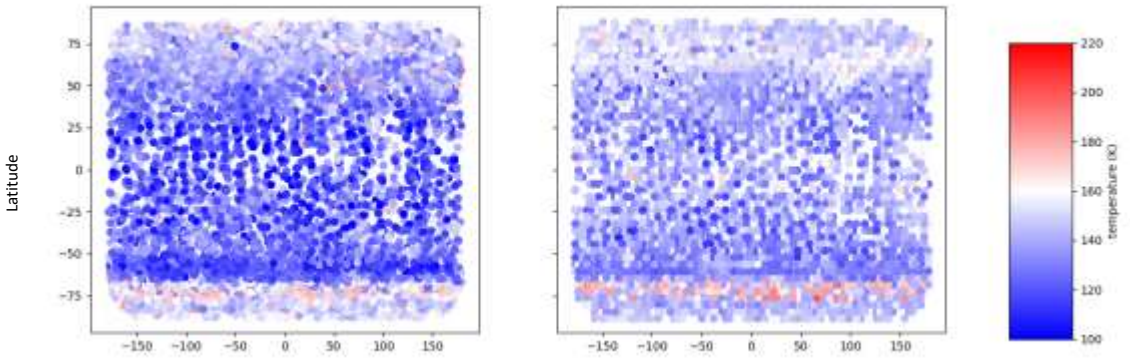

Figure 6 Longitude/Latitude distribution of ACS-NIR observations (left) and GEM-Mars temperatures (right) from the 2nd half of MY34 through to the first half of MY36.

Impact of non-orographic scheme on temperatures

New simulations with different parameters relating to the non-orographic gravity wave drag parameterisation were performed to address the temperature bias in the model. Figure 7 and Figure 8 show the impact of the scheme on simulated temperatures. In Figure 7, we show the zonal mean temperature differences between a simulation with the non-orographic scheme off and with the scheme on at the 4 cardinal seasons. The red colours indicate that when the non-orographic GW scheme is turned off, temperatures are warmer, so the scheme has a cooling effect in those regions. Where it is a blue shade, these are regions where the scheme causes a warming effect. Note that the scheme itself does not change the temperature, it only adjusts the wind speeds, and the thermal effect is then seen as a result of the dynamical effect. The largest impact of the scheme with the current settings occurs in the polar winter seasons, with a larger impact in the northern hemisphere, during the northern winter.

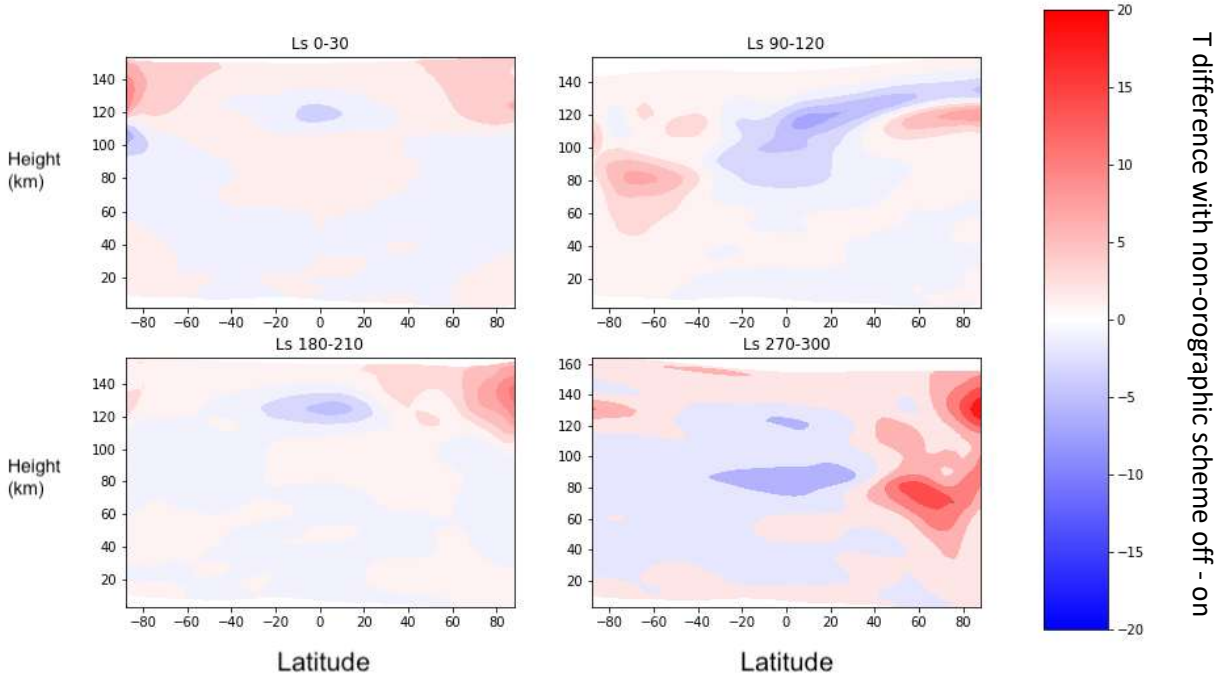

Figure 7 Latitude/Altitude zonal mean of temperature differences between GEM-Mars simulations with the non-orographic gravity wave scheme turned off – on for 4 seasons of MY35. Red indicates the scheme has a cooling effect on temperatures (they are higher when the scheme is off) and blue indicates a warming effect from the scheme.

In Figure 8, we show a similar stem plot as Figure 5, for temperature differences between NOMAD and GEM-Mars, with the 2 simulations, non-orographic on (green) and off (red). The bias is reduced in the southern winter, but more testing is needed.

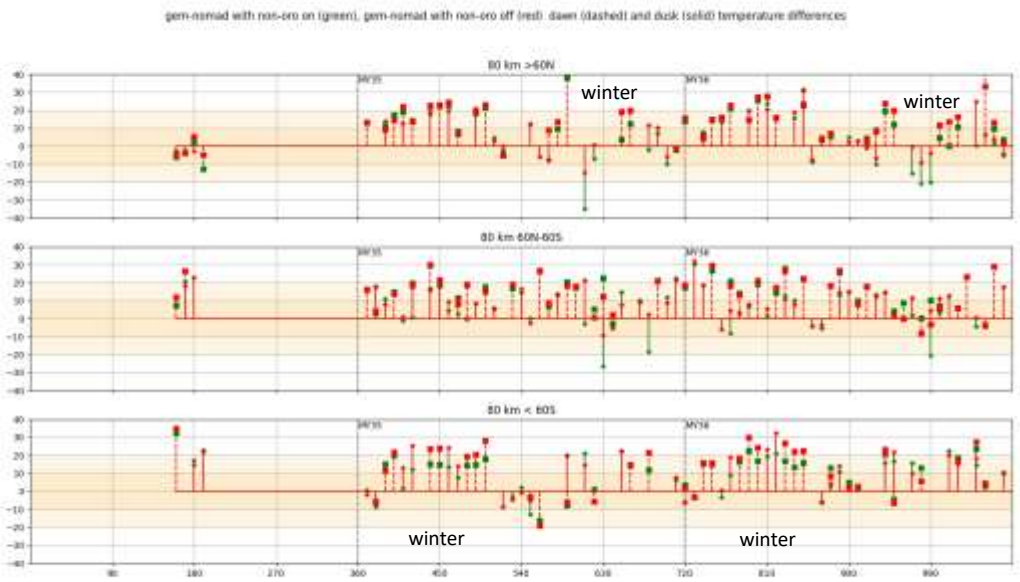

Figure 8 Stem plot showing the temperature differences between GEM-Mars and NOMAD with the scheme on (green) and the scheme off (red).

Impact of non-local thermodynamic equilibrium conditions

Another important factor influencing the thermal structure in this region is the presence of non-local thermodynamic equilibrium (NLTE) conditions, which occur above approximately 80 km altitude. In the troposphere and lower mesosphere, the atmosphere is in local thermodynamic equilibrium (LTE). In this state, molecular collisions happen frequently enough to evenly distribute absorbed radiant energy before it is emitted again. However, in the lower thermosphere, the atmospheric density drops significantly, reducing the frequency of molecular collisions. As a result, thermodynamic equilibrium can no longer be maintained. In this region, the exchange of energy between carbon dioxide (CO_2) and other molecules—particularly atomic oxygen (O)—is no longer in thermal equilibrium. Collisions with atomic oxygen become essential for exciting the vibrational levels of CO_2. Under NLTE conditions, radiation at a wavelength of 15 µm becomes especially important for radiative cooling. The efficiency of this cooling depends on the abundance of atomic oxygen and the rate at which CO_2 vibrational energy is quenched by O—parameters that are not well constrained in current GCMs (Medvedev et al., 2015).

We include the effects of NLTE conditions on temperature based on the original work of Lopez-Valverde et al. [1994a; 1994b]. This involves using a climatological profile of atomic oxygen interpolated onto the model vertical grid. As GEM-Mars computes the photochemistry of the atmosphere, we can connect it to the radiative transfer calculation and use a more realistic profile in our simulations. Preliminary tests with a one-dimensional version of the model chemistry and physics indicate that using the model profile shifts the cooling to a lower altitude, with a magnitude difference of ~30 K. This is promising, as the simulations are often too warm compared with NOMAD in the 80 km region. Figure 9 gives a timeseries of altitude profiles for 3 latitude bands (60N, equator and 60S) of temperature differences between and simulation with the old formulation and the new formulation using the modelled profiles of atomic oxygen. As expected, the effects are at and above 80 km, where the simulation with the new formulation is cooler between 80-110 km (blue) and warmer above (red). This figure shows the overall impact on the simulation while Figure 10 has model values extracted at NOMAD diffraction order 148 observation times and locations. Again, the blue regions indicate that the new formulation is cooler than the old and vice-versa for red regions. It is more difficult to see the impact of NLTE changes at the altitudes where order 148 is sensitive (below 80 km) but there are some differences, mostly in the winter polar regions where the differences reach to lower altitudes in Figure 9.

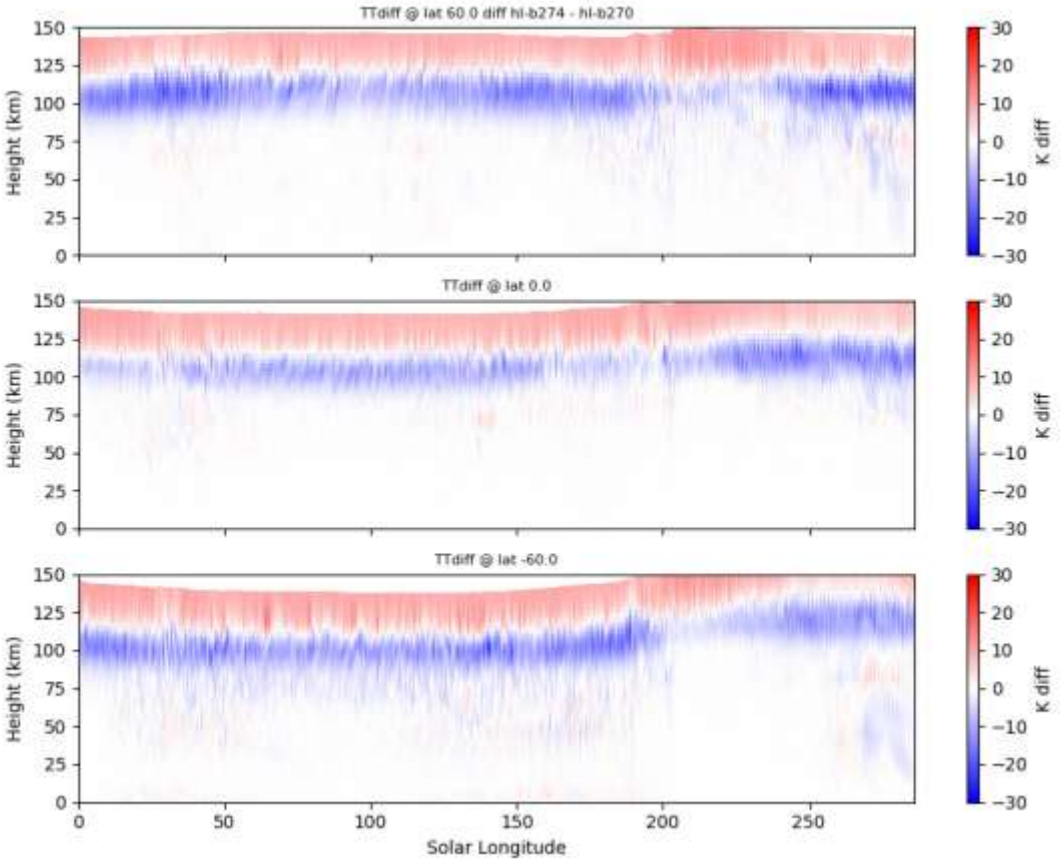

Figure 9 Temperature difference between new NLTE method and old for one Mars year at 3 different latitude bands (60N, EQ, 60S). Blue shading indicates that the new method using model values of atomic oxygen is cooler than the old method using a climatology. The model was previously over-predicting temperatures in this region.

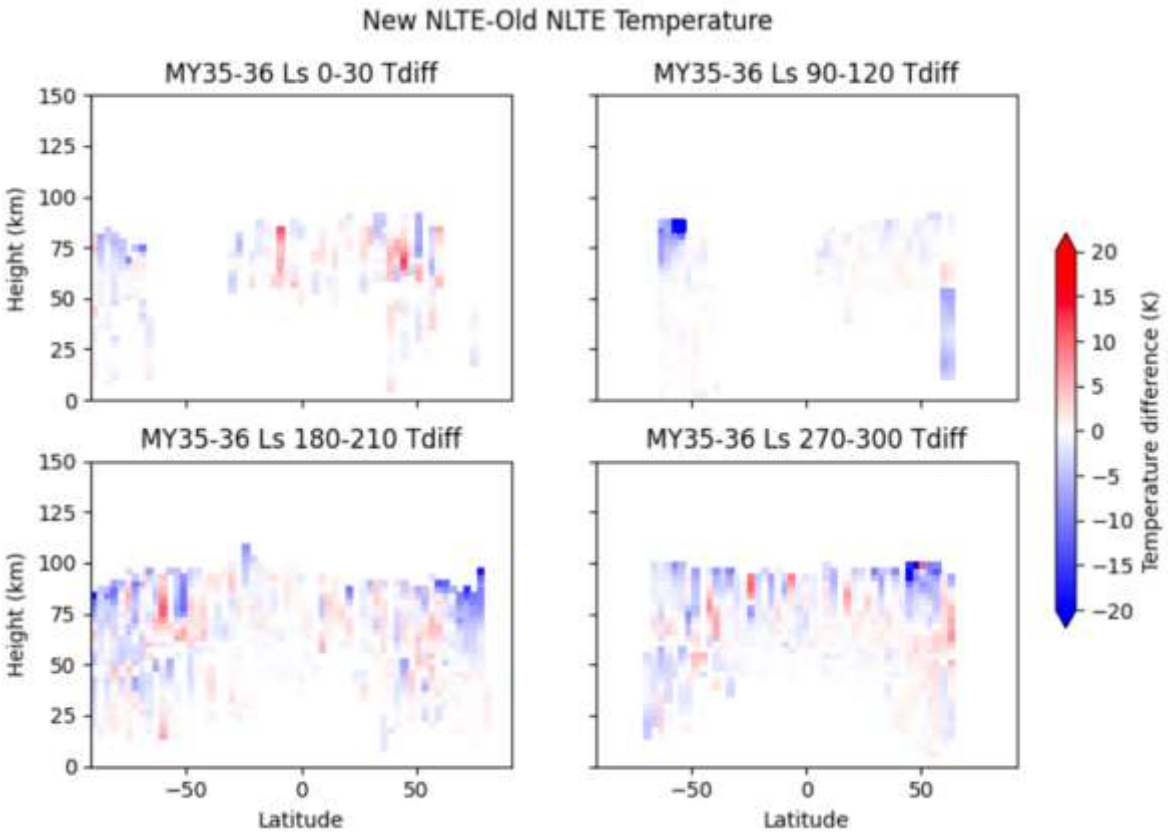

Figure 10 Difference in model temperatures (same as Figure 9) extracted at NOMAD observation times and locations (orders 148 and 132). Blue indicates that the new formulation is cooler than the old.

After the modification to the NLTE code, we compared to the observed NOMAD temperatures for orders 165, 148 and 132 with the full profiles from the model (using order 148 times and locations) for 2 seasons (split into sunrise and sunset occultations) as shown in Figure 11. Overall, the model temperatures follow the observed patterns and are within a reasonable range. The second half of the year mesopause temperatures are warmer in the model than observed, but we are on the edge of the observation sensitivity.

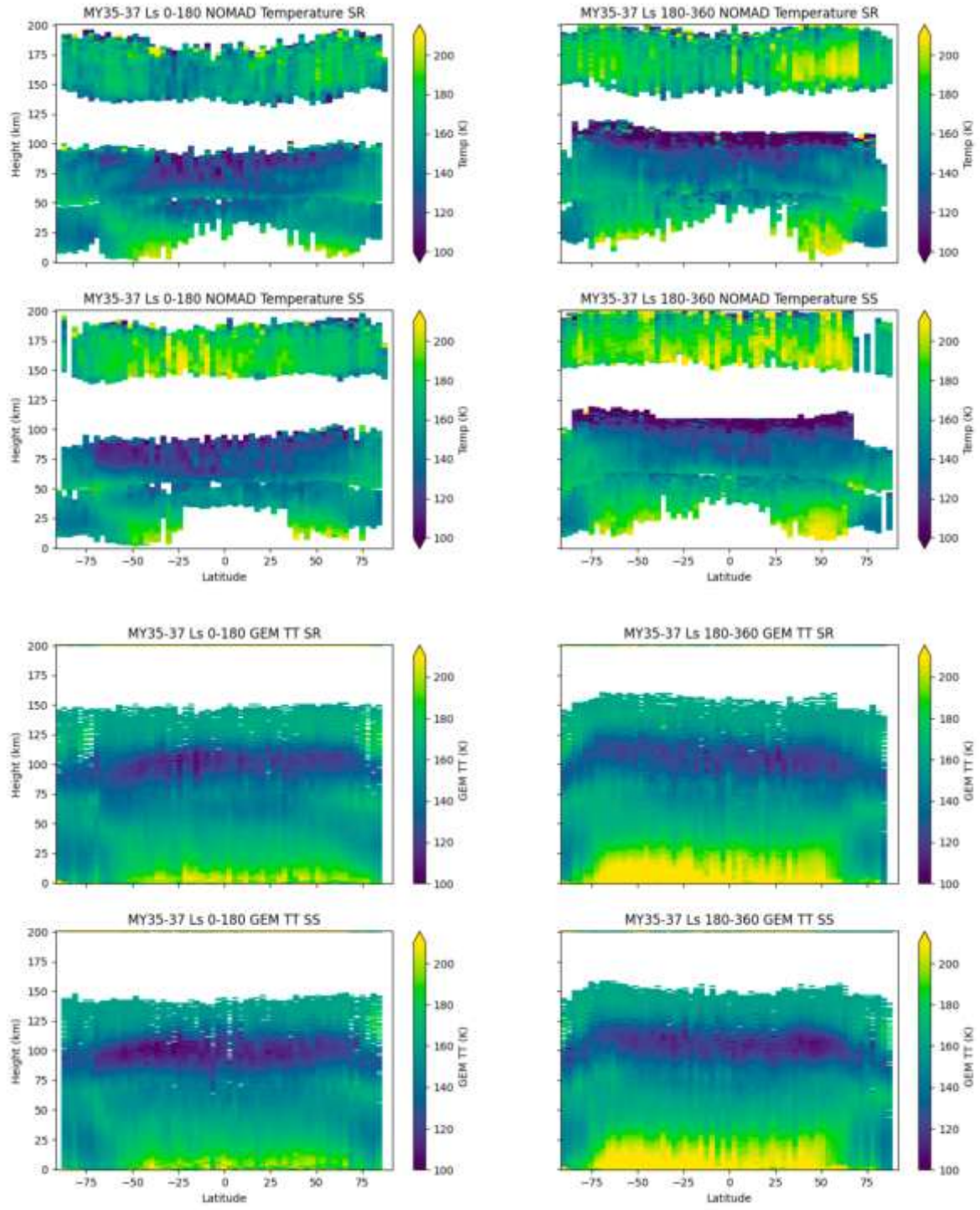

Figure 11 Zonal mean temperature comparison for 2 seasons, split into sunrise (SR) and sunset (SS) occultations. The top four plots show NOMAD temperatures for orders 165, 148 and 132. The lower four plots show the GEM-Mars full profiles extracted at the times and locations of the order 148 observations (between 50-100 km).

Searching for gravity waves in the NOMAD data

In Figure 12, we look at latitude-altitude plots for all order 148 occultations during MY35-37, divided into the 1st (left column) and 2nd half (right column) of the year. We divide the occultations again into sunrise (top 3 rows) and sunset (bottom 3 rows). In each set of plots, we show zonal mean temperature (top), the mean normalized temperature perturbations (middle) and the number of

occultations used to make the mean (bottom) to help identify the statistical significance. Here we can see some differences between sunrise and sunset, for example, just south of the equator in the first half of the year, there is more activity in the sunset occultations. Between 40-65°N in the 2nd half of the year, there appears to be more activity in the sunrise occultations (indicated with red circles).

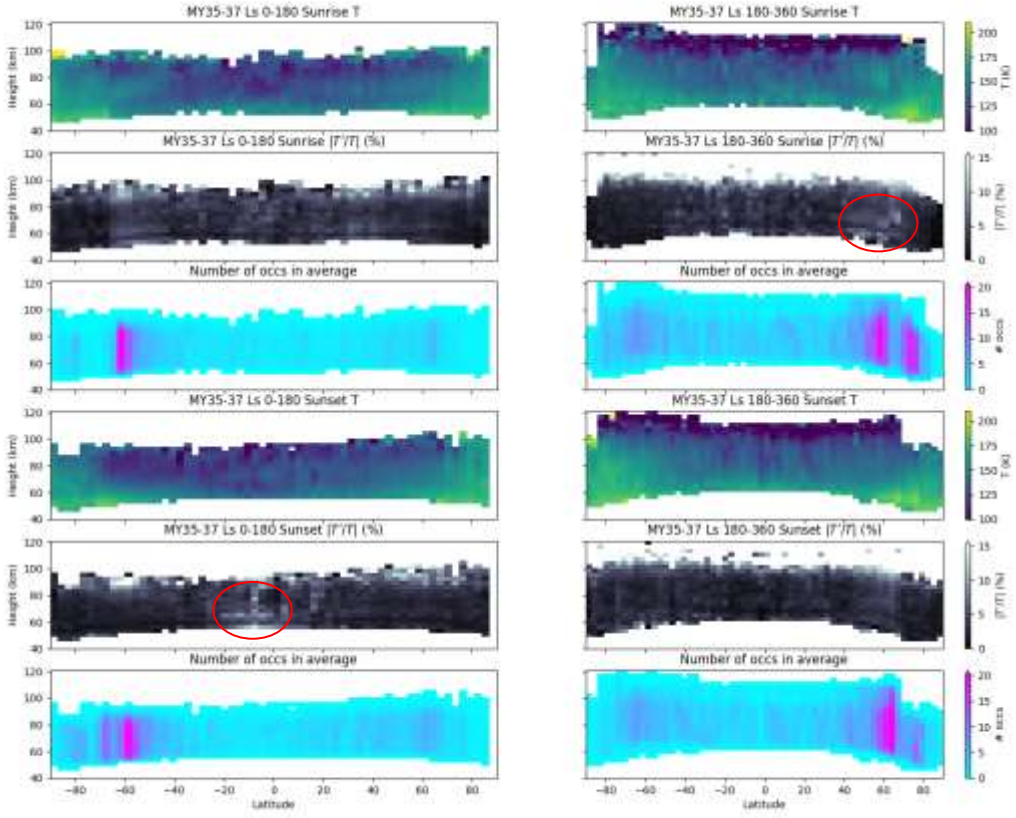

Figure 12 Zonal mean profiles of temperature, normalized perturbations and the number of occultations used in the mean. The left column is the 1st half of the year, and the right column is the 2nd half. The top 3 plots are for sunrise occultations and the bottom 3 are for sunset. The red circles highlight regions of increased perturbations.

From the mean and wave components of the profiles, we can then look at the wave amplitudes, potential energy, the Brunt-Väisälä frequency (N^2), momentum fluxes and drag on the mean flow as described in Section 3. Figure 13 shows one example profile analysis, using a NOMAD order 148 observation, taken in MY35, Ls=59.11 (2019/07/29) at latitude 62.17°S. The first frame shows the temperature profile in solid blue with the shaded error and the fitted background temperature in dashed blue. We include the full GEM-Mars profile in green along with its fitted background. The middle frame shows the amplitude of the power spectrum with the strongest wave amplitudes around 2.5-3.0 K and wavenumbers grouped at the lower end of the spectrum, indicating longer wavelengths, between 1-10 km. In the last frame, the blue profile is the estimated drag on the mean flow due to these gravity waves. In green, we show the calculated absolute value of the gravity wave drag from the two schemes in the model. In this example, the order of magnitude of the GWD for the observation and model is on the same order, although the observation peak drag is slightly above the non-orographic drag value and slightly below the smaller peak of the non-orographic drag.

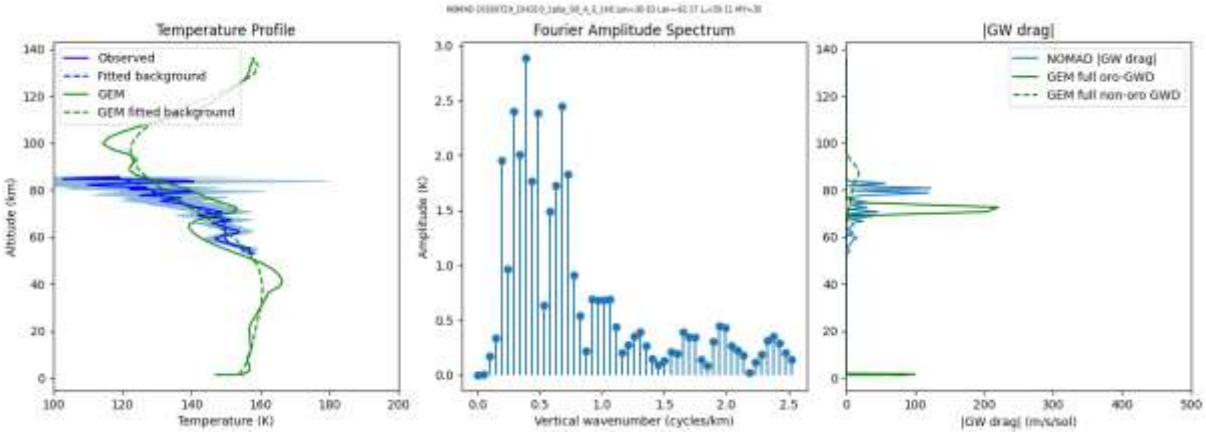

Figure 13 One example profile from NOMAD order 148, taken in MY35, L_s=59.11 (2019/07/29) at latitude 62.17°S. The first frame shows the temperature profile in solid blue with the shaded error and the fitted background temperature in dashed blue. We include the full GEM-Mars profile in green along with its fitted background. The middle frame shows the amplitude of the power spectrum with the strongest wave amplitudes around 2.5-3.0 K and wavenumbers grouped at the lower end of the spectrum, indicating longer wavelengths, between 1-10 km. In the last frame, the blue profile is the estimated drag on the mean flow due to these gravity waves. In green, we show the calculated absolute value of the gravity wave drag from the two schemes in the model.

We then take all the profiles of GWD estimated from NOMAD for orders 148 and 132 and calculated by GEM-Mars and analyse the zonal means as shown in Figure 14. Like the temperature plot of Figure 11, we divide the data into 2 seasons and SR/SS occultations. Both NOMAD and GEM-Mars show more activity in the sunrise occultations in the first half of the year in the southern hemisphere. This behaviour is more difficult to distinguish in the second half of the year in the northern hemisphere where there is stronger activity in both the SR and SS occultations.

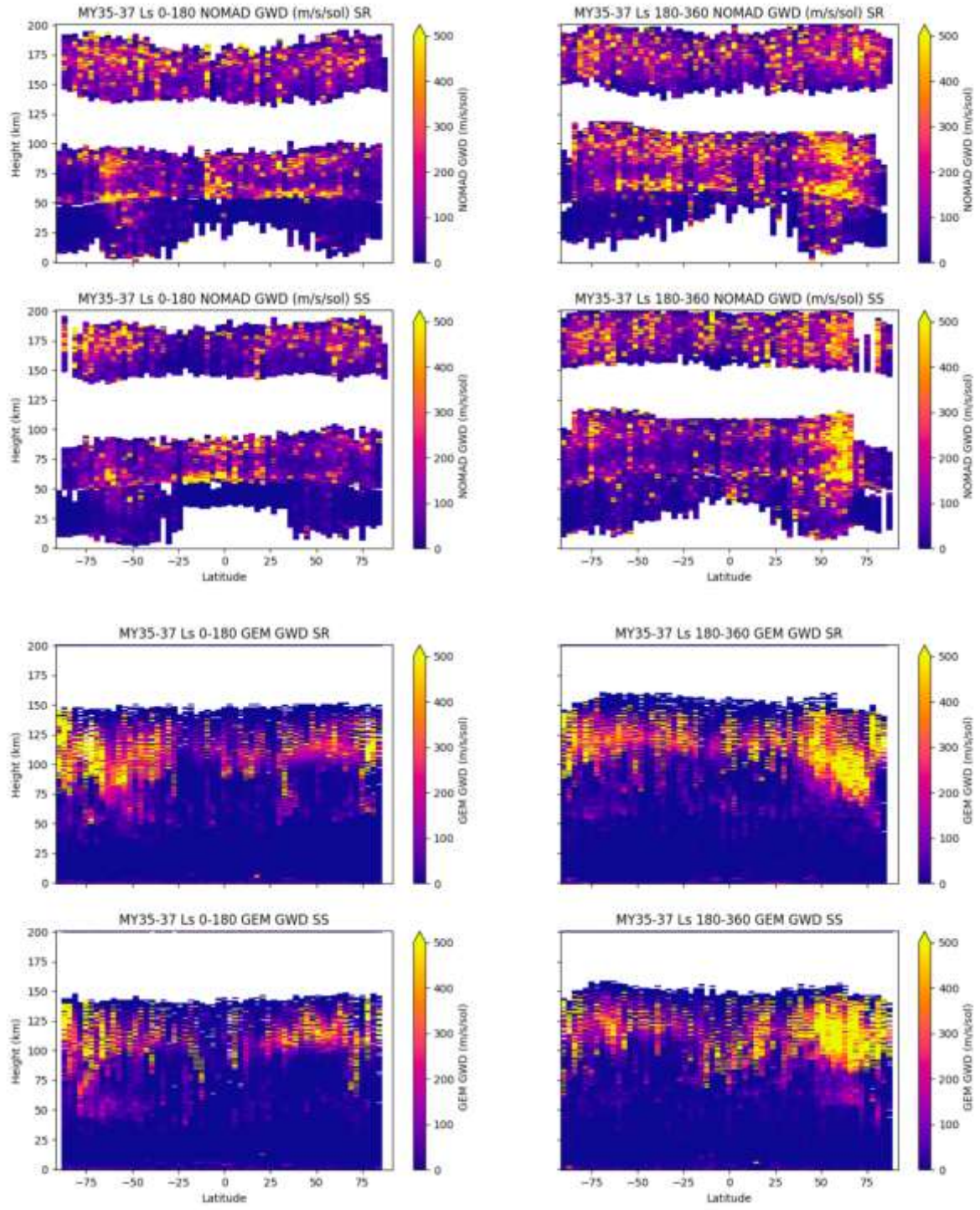

Figure 14 Zonal mean GWD amplitude comparison for 2 seasons, split into sunrise (SR) and sunset (SS) occultations. The top four plots show NOMAD GWD estimated for orders 165, 148 and 132. The lower four plots show the GEM-Mars full profiles of both orographic and non-orographic wave drag combined, extracted at the times and locations of the order 148 observations (between 50-100 km).

Implications for the formation of CO_2 ice clouds

We are also analysing the NOMAD profiles to see where CO_2 ice clouds might form. Figure 15 shows one particular profile where the temperature drops below the CO_2 frost point and we are investigating the potential to use NOMAD retrievals of aerosols and CO_2 ice clouds such as those done by Flimon et

al. (2025) and Luizzi et al. (2021) to see if the clouds themselves were observed when the temperatures are cold enough. We also show the GEM-Mars profiles from the high- and low-resolution simulations. Both simulations drop below the frost point but at a higher altitude. This analysis will help as we implement the formation of CO_2 ice clouds in the GCM.

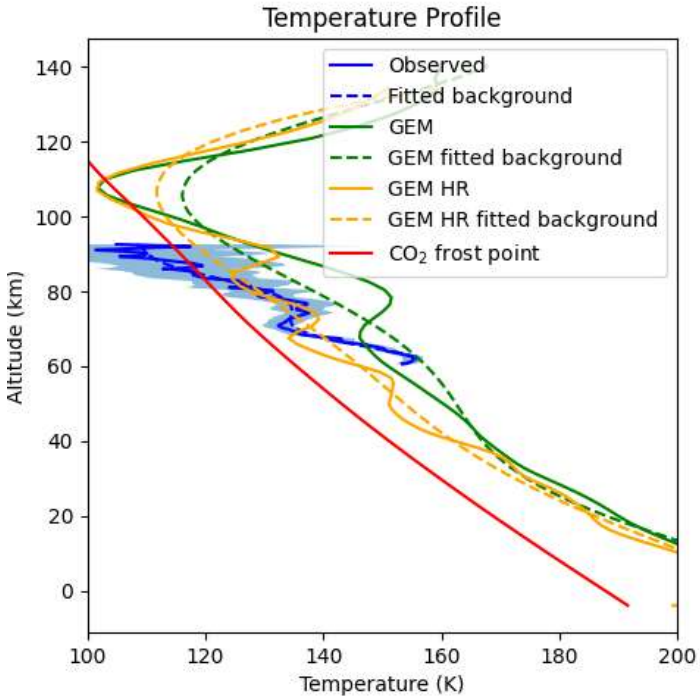

Figure 15 profile for NOMAD temperature profile taken on 18/02/2021 (MY36 L_s=5.5 at 35N, 198E) in blue, GEM-Mars low resolution in green, high resolution in orange. The red line indicates the CO_2 saturation vapour pressure.

Conclusions and future work

We see gravity waves frequently in the TGO/NOMAD observations and are building a climatology of activity over several Martian years. We see some differences in sunrise and sunset behaviour, particularly in the southern hemisphere winter.

By analysing the temperatures and wave activity observed by NOMAD, we have been able to tune the GEM-Mars GCM parameterisations of gravity wave drag to better match the observations and provide more realistic simulations. There are still some possible improvements to make, such as making the non-orographic wave launching level more dynamic, based on the atmospheric conditions and the position of the planetary boundary layer.

We are continuing the analysis and tuning of the model, with more high-resolution simulations planned to understand better the seasonal and diurnal differences in wave activity. The analysis temperatures and wave activity looking for the potential for CO_2 ice cloud formation and the implementation of a co2 ice cloud scheme is underway.

This project has also allowed for other improvements to the model, such as the implementation of a better formulation for the radiative transfer in non-local thermodynamic equilibrium conditions.

There are 2 papers in preparation based on this work, to be submitted in the following months.

Bibliography

Altieri, F., Spiga, A., Zasova, L., Bellucci, G., Bibring, J.-P., 2012. Gravity waves mapped by the OMEGA/MEX instrument through O_2 dayglow at 1.27 μ m: Data analysis and atmospheric modeling: MARS, GRAVITY WAVES MAPPED BY O_2 DAYGLOW. Journal of Geophysical Research: Planets 117, n/a-n/a. https://doi.org/10.1029/2012JE004065

Belyaev, D.A., Fedorova, A.A., Trokhimovskiy, A., Alday, J., Korablev, O.I., Montmessin, F., Starichenko, E.D., Olsen, K.S., Patrakeev, A.S., 2022. Thermal Structure of the Middle and Upper Atmosphere of Mars From ACS/TGO CO2 Spectroscopy. Journal of Geophysical Research: Planets 127, e2022JE007286. https://doi.org/10.1029/2022JE007286

Chaffin, M.S., Deighan, J., Schneider, N.M., Stewart, A.I.F., 2017. Elevated atmospheric escape of atomic hydrogen from Mars induced by high-altitude water. Nature Geoscience 10, 174–178. https://doi.org/10.1038/ngeo2887

Charron, M., Manzini, E., Warner, C.D., 2002. Intercomparison of gravity wave parameterizations: Hines Doppler-spread and Warner and McIntyre ultra-simple schemes. J. of the Met. Soc. of Japan. No. 3, Vol 80, pp. 335–345.

Clancy, R.T., Wolff, M.J., Heavens, N.G., James, P.B., Lee, S.W., Sandor, B.J., Cantor, B.A., Malin, M.C., Tyler, D., Spiga, A., 2021. Mars perihelion cloud trails as revealed by MARCI: Mesoscale topographically focused updrafts and gravity wave forcing of high altitude clouds. Icarus 362, 114411. https://doi.org/10.1016/j.icarus.2021.114411

Côté, J., Desmarais, J.-G., Gravel, S., Méthot, A., Patoine, A., Roch, M., Staniforth, A., 1998b. The operational CMC-MRB global environmental multiscale (GEM) model. Part II: Results. Monthly Weather Review 126, 1397–1418.

Côté, J., Gravel, S., Méthot, A., Patoine, A., Roch, M., Staniforth, A., 1998a. The operational CMC-MRB global environmental multiscale (GEM) model. Part I: Design considerations and formulation. Monthly Weather Review 126, 1373–1395.

Creasey, J.E., Forbes, J.M., Keating, G.M., 2006. Density variability at scales typical of gravity waves observed in Mars' thermosphere by the MGS accelerometer. Geophys. Res. Lett. 33, L22814. https://doi.org/10.1029/2006GL027583

Daerden, F., Neary, L., Villanueva, G., Liuzzi, G., Aoki, S., Clancy, R.T., Whiteway, J.A., Sandor, B.J., Smith, M.D., Wolff, M.J., Pankine, A., Khayat, A., Novak, R., Cantor, B., Crismani, M., Mumma, M.J., Viscardy, S., Erwin, J., Depiesse, C., Mahieux, A., Piccialli, A., Robert, S., Trompet, L., Willame, Y., Neefs, E., Thomas, I.R., Ristic, B., Vandaele, A.C., 2022. Explaining NOMAD D/H Observations by Cloud-Induced Fractionation of Water Vapor on Mars. Journal of Geophysical Research: Planets 127, e2021JE007079. https://doi.org/10.1029/2021JE007079

England, S.L., Liu, G., Yiğit, E., Mahaffy, P.R., Elrod, M., Benna, M., Nakagawa, H., Terada, N., Jakosky, B., 2017. MAVEN NGIMS observations of atmospheric gravity waves in the Martian thermosphere: Gravity Wave Observations at Mars. Journal of Geophysical Research: Space Physics. https://doi.org/10.1002/2016JA023475

Flimon, Z., Erwin, J., Robert, S., Neary, L., Piccialli, A., Trompet, L., Willame, Y., Vanhellemont, F., Daerden, F., Bauduin, S., Wolff, M., Thomas, I.R., Ristic, B., Mason, J.P., Depiesse, C., Patel, M.R., Bellucci, G., Lopez-Moreno, J.-J., Vandaele, A.C., 2025. Aerosol Climatology on Mars as Observed by NOMAD UVIS on ExoMars TGO. Journal of Geophysical Research: Planets 130, e2024JE008303. https://doi.org/10.1029/2024JE008303

Fritts, D.C., Wang, L., Tolson, R.H., 2006. Mean and gravity wave structures and variability in the Mars upper atmosphere inferred from Mars Global Surveyor and Mars Odyssey aerobraking densities. Journal of Geophysical Research 111. https://doi.org/10.1029/2006JA011897

Gilli, G., Forget, F., Spiga, A., Navarro, T., Millour, E., Montabone, L., Kleinböhl, A., Kass, D.M., McCleese, D.J., Schofield, J.T., 2020. Impact of gravity waves on the middle atmosphere of Mars: a non-orographic gravity wave parameterization based on Global Climate modeling and MCS observations. Journal of Geophysical Research: Planets 125, e2018JE005873. https://doi.org/10.1029/2018JE005873

González-Galindo, F., Määttänen, A., Forget, F., Spiga, A., 2011. The martian mesosphere as revealed by CO2 cloud observations and General Circulation Modeling. Icarus 216, 10–22. https://doi.org/10.1016/j.icarus.2011.08.006

Guzewich, S.D., de la Torre Juárez, M., Newman, C.E., Mason, E., Smith, M.D., Miller, N., Khayat, A.S.J., Kahanpää, H., Viúdez-Moreiras, D., Richardson, M.I., 2021. Gravity Wave Observations by the Mars Science Laboratory REMS Pressure Sensor and Comparison With Mesoscale Atmospheric Modeling With MarsWRF. Journal of Geophysical Research: Planets 126, e2021JE006907. https://doi.org/10.1029/2021JE006907

Heavens, N.G., Kass, D.M., Kleinböhl, A., Schofield, J.T., 2020. A multiannual record of gravity wave activity in Mars's lower atmosphere from on-planet observations by the Mars Climate Sounder. Icarus 341, 113630. https://doi.org/10.1016/j.icarus.2020.113630

Hines, C., 1997a. Doppler-spread parameterization of gravity-wave momentum deposition in the middle atmosphere. Journal of Atmospheric and Solar-Terrestrial Physics 59.

Hines, C.O., 1997b. Doppler-spread parameterization of gravity-wave momentum deposition in the middle atmosphere. Part 2: Broad and quasi monochromatic spectra, and implementation. Journal of Atmospheric and Solar-Terrestrial Physics 59, 387–400.

Hines, C.O., 2004. The Doppler spread theory and parameterization revisited. Journal of Atmospheric and Solar-Terrestrial Physics 66, 949–956. https://doi.org/10.1016/j.jastp.2004.02.005

Korablev, O., Montmessin, F., Trokhimovskiy, A., Fedorova, A.A., Shakun, A.V., Grigoriev, A.V., Moshkin, B.E., Ignatiev, N.I., Forget, F., Lefèvre, F., Anufreychik, K., Dzuban, I., Ivanov, Y.S., Kalinnikov, Y.K., Kozlova, T.O., Kungurov, A., Makarov, V., Martynovich, F., Maslov, I., Merzlyakov, D., Moiseev, P.P., Nikolskiy, Y., Patrakeev, A., Patsaev, D., Santos-Skripko, A., Sazonov, O., Semena, N., Semenov, A., Shashkin, V., Sidorov, A., Stepanov, A.V., Stupin, I., Timonin, D., Titov, A.Y., Viktorov, A., Zharkov, A., Altieri, F., Arnold, G., Belyaev, D.A., Bertaux, J.L., Betsis, D.S., Duxbury, N., Encrenaz, T., Fouchet, T., Gérard, J.-C., Grassi, D., Guerlet, S., Hartogh, P., Kasaba, Y., Khatuntsev, I., Krasnopolsky, V.A., Kuzmin, R.O., Lellouch, E., Lopez-Valverde, M.A., Luginin, M., Määttänen, A., Marcq, E., Martin Torres, J., Medvedev, A.S., Millour, E., Olsen, K.S., Patel, M.R., Quantin-Nataf, C., Rodin, A.V., Shematovich, V.I., Thomas, I., Thomas, N., Vazquez, L., Vincendon, M., Wilquet, V., Wilson, C.F., Zasova, L.V., Zelenyi, L.M., Zorzano, M.P., 2018. The Atmospheric Chemistry Suite (ACS) of Three Spectrometers for the ExoMars 2016 Trace Gas Orbiter. Space Sci Rev 214, 7. https://doi.org/10.1007/s11214-017-0437-6

Kuroda, T., Medvedev, A.S., Yiğit, E., 2020. Gravity Wave Activity in the Atmosphere of Mars During the 2018 Global Dust Storm: Simulations With a High-Resolution Model. Journal of Geophysical Research: Planets 125, e2020JE006556. https://doi.org/10.1029/2020JE006556

Kuroda, T., Medvedev, A.S., Yiğit, E., Hartogh, P., 2015. A global view of gravity waves in the Martian atmosphere inferred from a high-resolution general circulation model: GRAVITY WAVES ON MARS. Geophysical Research Letters 42, 9213–9222. https://doi.org/10.1002/2015GL066332

Lindzen, R.S., 1981. Turbulence and stress owing to gravity wave and tidal breakdown. Journal of Geophysical Research: Oceans 86, 9707–9714.
Listowski, C., Määttänen, A., Montmessin, F., Spiga, A., Lefèvre, F., 2014. Modeling the microphysics of CO2 ice clouds within wave-induced cold pockets in the martian mesosphere. Icarus 237, 239–261. https://doi.org/10.1016/j.icarus.2014.04.022
Liuzzi, G., Villanueva, G.L., Trompet, L., Crismani, M.M.J., Piccialli, A., Aoki, S., Lopez-Valverde, M.A., Stolzenbach, A., Daerden, F., Neary, L., Smith, M.D., Patel, M.R., Lewis, S.R., Clancy, R.T., Thomas, I.R., Ristic, B., Bellucci, G., Lopez-Moreno, J.-J., Vandaele, A.C., 2021. First Detection and Thermal Characterization of Terminator CO2 Ice Clouds With ExoMars/NOMAD. Geophysical Research Letters 48, e2021GL095895. https://doi.org/10.1029/2021GL095895
Lopez-Valverde, M.A., Lopez-Puertas, M., 1994a. A non-local thermodynamic equilibrium radiative transfer model for infrared emissions in the atmosphere of Mars 1. Theoretical basis and nighttime populations of vibrational levels. J. of Geophysical Research, Vol. 99, No. E6 pp. 13093-13115.
Lopez-Valverde, M.A., Lopez-Puertas, M., 1994b. A non-local thermodynamic equilibrium radiative transfer model for infrared emissions in the atmosphere of Mars 2. Daytime populations of vibrational levels. J. Geophysical Research, Vol. 99, No. E6, pp. 13117-13132.
Lott, F., Guez, L., 2013. A stochastic parameterization of the gravity waves due to convection and its impact on the equatorial stratosphere. Journal of Geophysical Research: Atmospheres 118, 8897–8909. https://doi.org/10.1002/jgrd.50705
Lott, F., Guez, L., Maury, P., 2012. A stochastic parameterization of non-orographic gravity waves: Formalism and impact on the equatorial stratosphere. Geophysical Research Letters 39. https://doi.org/10.1029/2012GL051001
Lott, F., Miller, M.J., 1997 A new subgrid-scale orographic drag parameterization: Its formulation and testing. Q. J. R. Meteorol. Soc., 123, pp. 101-127.
Määttänen, A., Montmessin, F., Gondet, B., Scholten, F., Hoffmann, H., González-Galindo, F., Spiga, A., Forget, F., Hauber, E., Neukum, G., Bibring, J.-P., Bertaux, J.-L., 2010. Mapping the mesospheric CO2 clouds on Mars: MEx/OMEGA and MEx/HRSC observations and challenges for atmospheric models. Icarus 209, 452–469. https://doi.org/10.1016/j.icarus.2010.05.017
Mathé, C., Määttänen, A., Audouard, J., Listowski, C., Millour, E., Forget, F., Spiga, A., Bardet, D., Teinturier, L., Falletti, L., Vals, M., González-Galindo, F., Montmessin, F., 2021. Global 3D modelling of Martian CO2 clouds (No. EPSC2021-324). Presented at the EPSC2021, Copernicus Meetings. https://doi.org/10.5194/epsc2021-324
McFarlane, N.A., 1987. The effect of orographically excited gravity wave drag on the general circulation of the lower stratosphere and troposphere. Journal of the atmospheric sciences 44, 1775–1800.
Medvedev, A.S., González-Galindo, F., Yiğit, E., Feofilov, A.G., Forget, F., Hartogh, P., 2015. Cooling of the Martian thermosphere by CO2 radiation and gravity waves: An intercomparison study with two general circulation models. J. Geophys. Res. Planets 120, 2015JE004802. https://doi.org/10.1002/2015JE004802
Medvedev, A.S., Yiğit, E., 2019. Gravity Waves in Planetary Atmospheres: Their Effects and Parameterization in Global Circulation Models. Atmosphere 10, 531. https://doi.org/10.3390/atmos10090531
Neary, L., Daerden, F., Aoki, S., Whiteway, J., Clancy, R.T., Smith, M., Viscardy, S., Erwin, J.T., Thomas, I.R., Villanueva, G., Liuzzi, G., Crismani, M., Wolff, M., Lewis, S.R., Holmes, J.A., Patel, M.R., Giuranna, M., Depiesse, C., Piccialli, A., Robert, S., Trompet, L., Willame, Y., Ristic, B., Vandaele, A.C., 2020.

Explanation for the Increase in High-Altitude Water on Mars Observed by NOMAD During the 2018 Global Dust Storm. Geophysical Research Letters 47, e2019GL084354. https://doi.org/10.1029/2019GL084354

Neefs, E., Vandaele, A.C., Drummond, R., Thomas, I.R., Berkenbosch, S., Clairquin, R., Delanoye, S., Ristic, B., Maes, J., Bonnewijn, S., Pieck, G., Equeter, E., Depiesse, C., Daerden, F., Ransbeeck, E.V., Nevejans, D., Rodriguez-Gómez, J., López-Moreno, J.-J., Sanz, R., Morales, R., Candini, G.P., Pastor-Morales, M.C., Aparicio Del Moral, B., Jeronimo-Zafra, J.-M., Gómez-López, J.M., Alonso-Rodrigo, G., Pérez-Grande, I., Cubas, J., Gomez-Sanjuan, A.M., Navarro-Medina, F., Thibert, T., Patel, M.R., Bellucci, G., De Vos, L., Lesschaeve, S., Vooren, N.V., Moelans, W., Aballea, L., Glorieux, S., Baeke, A., Kendall, D., De Neef, J., Soenen, A., Puech, P.-Y., Ward, J., Jamoye, J.-F., Diez, D., Vicario-Arroyo, A., Jankowski, M., 2015. NOMAD spectrometer on the ExoMars trace gas orbiter mission: part 1—design, manufacturing and testing of the infrared channels. Appl. Opt. 54, 8494. https://doi.org/10.1364/AO.54.008494

Palmer, T.N., Shutts, G.J., Swinbank,R., 1986. Alleviation of a systematic westerly bias in general circulation and numerical weather prediction models through an orographic gravity wave drag parameterization. Quarterly Journal of the Royal Meteorological Society 112, 1001–1039.

Spiga, A., González-Galindo, F., López-Valverde, M.-á., Forget, F., 2012. Gravity waves, cold pockets and CO_2 clouds in the Martian mesosphere: GW AND COLD POCKETS IN MARS MESOSPHERE. Geophysical Research Letters 39, n/a-n/a. https://doi.org/10.1029/2011GL050343

Starichenko, E.D., Belyaev, D.A., Medvedev, A.S., Fedorova, A.A., Korablev, O.I., Trokhimovskiy, A., Yiğit, E., Alday, J., Montmessin, F., Hartogh, P., 2021. Gravity Wave Activity in the Martian Atmosphere at Altitudes 20–160 km From ACS/TGO Occultation Measurements. Journal of Geophysical Research: Planets 126, e2021JE006899. https://doi.org/10.1029/2021JE006899

Starichenko, E.D., Medvedev, A.S., Belyaev, D.A., Yiğit, E., Fedorova, A.A., Korablev, O.I., Trokhimovskiy, A., Montmessin, F., Hartogh, P., 2024. Climatology of gravity wave activity based on two Martian years from ACS/TGO observations. A&A 683, A206. https://doi.org/10.1051/0004-6361/202348685

Stone, S.W., Yelle, R.V., Benna, M., Lo, D.Y., Elrod, M.K., Mahaffy, P.R., 2020. Hydrogen escape from Mars is driven by seasonal and dust storm transport of water. Science 370, 824–831. https://doi.org/10.1126/science.aba5229

Trompet, L., Vandaele, A.C., Thomas, I., Aoki, S., Daerden, F., Erwin, J., Flimon, Z., Mahieux, A., Neary, L., Robert, S., Villanueva, G., Liuzzi, G., López-Valverde, M.A., Brines, A., Bellucci, G., López-Moreno, J.J., Patel, M.R., 2023a. Carbon Dioxide Retrievals From NOMAD-SO on ESA's ExoMars Trace Gas Orbiter and Temperature Profiles Retrievals With the Hydrostatic Equilibrium Equation: 1. Description of the Method. Journal of Geophysical Research: Planets 128, e2022JE007277. https://doi.org/10.1029/2022JE007277

Trompet, L., Vandaele, A.C., Thomas, I., Aoki, S., Daerden, F., Erwin, J., Flimon, Z., Mahieux, A., Neary, L., Robert, S., Villanueva, G., Liuzzi, G., López-Valverde, M.A., Brines, A., Bellucci, G., Lopez-Moreno, J.J., Patel, M.R., 2023b. Carbon Dioxide Retrievals From NOMAD-SO on ESA's ExoMars Trace Gas Orbiter and Temperature Profile Retrievals With the Hydrostatic Equilibrium Equation: 2. Temperature Variabilities in the Mesosphere at Mars Terminator. JGR Planets 128, e2022JE007279. https://doi.org/10.1029/2022JE007279

Vals, M., Spiga, A., Forget, F., Millour, E., Montabone, L., Lott, F., 2019. Study of gravity waves distribution and propagation in the thermosphere of Mars based on MGS, ODY, MRO and MAVEN

density measurements. Planetary and Space Science 104708. https://doi.org/10.1016/j.pss.2019.104708

Villanueva, G.L., Liuzzi, G., Crismani, M.M.J., Aoki, S., Vandaele, A.C., Daerden, F., Smith, M.D., Mumma, M.J., Knutsen, E.W., Neary, L., Viscardy, S., Thomas, I.R., Lopez-Valverde, M.A., Ristic, B., Patel, M.R., Holmes, J.A., Bellucci, G., Lopez-Moreno, J.J., NOMAD team, 2021. Water heavily fractionated as it ascends on Mars as revealed by ExoMars/NOMAD. Sci. Adv. 7, eabc8843. https://doi.org/10.1126/sciadv.abc8843

Yeh, K.-S., Côté, J., Gravel, S., Méthot, A., Patoine, A., Roch, M., Staniforth, A., 2002. The CMC–MRB Global Environmental Multiscale (GEM) Model. Part III: Nonhydrostatic Formulation. Monthly weather review 130.

Yiğit, E., Aylward, A.D., Medvedev, A.S., 2008. Parameterization of the effects of vertically propagating gravity waves for thermosphere general circulation models: Sensitivity study. J. Geophys. Res. 113, D19106. https://doi.org/10.1029/2008JD010135

Yiğit, E., Medvedev, A.S., Benna, M., Jakosky, B.M., 2021. Dust Storm-Enhanced Gravity Wave Activity in the Martian Thermosphere Observed by MAVEN and Implication for Atmospheric Escape. Geophys Res Lett 48. https://doi.org/10.1029/2020GL092095

Yiğit, E., Medvedev, A.S., Hartogh, P., 2015. Gravity waves and high-altitude CO2 ice cloud formation in the Martian atmosphere. Geophys. Res. Lett. 42, 2015GL064275. https://doi.org/10.1002/2015GL064275

Zadra, A., Roch, M., Laroche, S., Charron, M., 2003. The subgrid-scale orographic blocking parametrization of the GEM Model. Atmosphere-Ocean 41, 155–170. https://doi.org/10.3137/ao.410204

5. DISSEMINATION AND VALORISATION

TGO/NOMAD SWT23, Matsushima, Japan, discussions with NOMAD team and follow-up committee, March 2023.

LUCA School of Arts, Brussels, Belgium, presentation on the Atmosphere of Mars, TGO/NOMAD and GCM modelling, March 2023

EGU 2023, Vienna, Austria (virtual participation), co-convener of session on Mars Science and Exploration, April 2023

The 3rd China-ESA Mars Advanced School, Beijing, China, invited speaker on Modelling Atmospheric Dynamics and Chemistry, May 2023

TGO/NOMAD SWT24, Potenza, Italy, discussions with NOMAD team and follow-up committee, September 2023.

Dust on Mars, RoadMap workshop, Brussels, Belgium, presentation on GCM modelling of dust transport and radiative effects, September 2023

Participation in an International Space Science Institute (ISSI) project titled “A multi-mission approach to close the gaps in understanding the structure and variability in the Mars upper Atmosphere”. The topic closely relates to this project and work was presented at the two in-person meetings in Bern, Switzerland in January 2024 and 2025.

In March 2024 the TGO/NOMAD SWT25 was held in Newcastle, UK, where results were presented. This provided an opportunity for discussions with NOMAD team and with the follow-up committee.

Invited seminar at Freie Universität in Berlin in June 2024. Presentations were given at the EuroPlanet Science Congress (EPSC) in Berlin in September 2024.

Participation in a workshop aimed at improving our knowledge on aerosols in the Martian atmosphere in Toulouse in September 2024.

6. PUBLICATIONS

Daerden, F., Crowley, J.N., Neary, L., Smith, M.D., Loeffler, M.J., Clancy, R.T., Wolff, M.J., Aoki, S., Sagawa, H., 2023. Heterogeneous Processes in the Atmosphere of Mars and Impact on H2O2 and O3 Abundances. Journal of Geophysical Research: Planets 128, e2023JE008014. https://doi.org/10.1029/2023JE008014

Gérard, J.-C., Soret, L., Hubert, B., Neary, L., Daerden, F., 2023. The brightness of the CO Cameron bands in the martian discrete aurora: A study based on revised cross sections. Icarus 402, 115602. https://doi.org/10.1016/j.icarus.2023.115602

Trompet, L., Vandaele, A.C., Thomas, I., Aoki, S., Daerden, F., Erwin, J., Flimon, Z., Mahieux, A., Neary, L., Robert, S., Villanueva, G., Liuzzi, G., López-Valverde, M.A., Brines, A., Bellucci, G., López-Moreno, J.J., Patel, M.R., 2023a. Carbon Dioxide Retrievals From NOMAD-SO on ESA's ExoMars Trace Gas Orbiter and Temperature Profiles Retrievals With the Hydrostatic Equilibrium Equation: 1. Description of the Method. Journal of Geophysical Research: Planets 128, e2022JE007277. https://doi.org/10.1029/2022JE007277

Trompet, L., Vandaele, A.C., Thomas, I., Aoki, S., Daerden, F., Erwin, J., Flimon, Z., Mahieux, A., Neary, L., Robert, S., Villanueva, G., Liuzzi, G., López-Valverde, M.A., Brines, A., Bellucci, G., Lopez-Moreno, J.J., Patel, M.R., 2023b. Carbon Dioxide Retrievals From NOMAD-SO on ESA's ExoMars Trace Gas Orbiter and Temperature Profile Retrievals With the Hydrostatic Equilibrium Equation: 2. Temperature Variabilities in the Mesosphere at Mars Terminator. JGR Planets 128, e2022JE007279. https://doi.org/10.1029/2022JE007279

Piccialli, A., Vandaele, A.C., Willame, Y., Määttänen, A., Trompet, L., Erwin, J.T., Daerden, F., Neary, L., Aoki, S., Viscardy, S., Thomas, I.R., Depiesse, C., Ristic, B., Mason, J.P., Patel, M.R., Wolff, M.J., Khayat, A.S.J., Bellucci, G., Lopez-Moreno, J.-J., 2023. Martian Ozone Observed by TGO/NOMAD-UVIS Solar Occultation: An Inter-Comparison of Three Retrieval Methods. Earth and Space Science 10, e2022EA002429. https://doi.org/10.1029/2022EA002429

Nakamura, Y., Leblanc, F., Terada, N., Hiruba, S., Murata, I., Nakagawa, H., Sakai, S., Aoki, S., Piccialli, A., Willame, Y., Neary, L., Vandaele, A.C., Murase, K., Kataoka, R., 2023. Numerical Prediction of Changes in Atmospheric Chemical Compositions During a Solar Energetic Particle Event on Mars. Journal of Geophysical Research: Space Physics 128, e2022JA031250. https://doi.org/10.1029/2022JA031250

Liuzzi, G., Villanueva, G.L., Aoki, S., Stone, S.W., Faggi, S., Trompet, L., Neary, L., Daerden, F., Viscardy, S., Masiello, G., Serio, C., Thomas, I.R., Patel, M.R., Bellucci, G., Lopez-Moreno, J.-J., Ristic, B., Vandaele, A.C., 2024. CO2 in the atmosphere of Mars depleted in 13C. Icarus 417, 116121. https://doi.org/10.1016/j.icarus.2024.116121

Martikainen, J., Muñoz, O., Gómez Martín, J.C., Passas Varo, M., Jardiel, T., Peiteado, M., Willame, Y., Neary, L., Becker, T., Wurm, G., 2025. Database of Martian dust optical properties in the UV-vis-NIR. Monthly Notices of the Royal Astronomical Society 537, 1489–1503. https://doi.org/10.1093/mnras/staf108

Flimon, Z., Erwin, J., Robert, S., Neary, L., Piccialli, A., Trompet, L., Willame, Y., Vanhellemont, F., Daerden, F., Bauduin, S., Wolff, M., Thomas, I.R., Ristic, B., Mason, J.P., Depiesse, C., Patel, M.R.,

Bellucci, G., Lopez-Moreno, J.-J., Vandaele, A.C., 2025. Aerosol Climatology on Mars as Observed by NOMAD UVIS on ExoMars TGO. Journal of Geophysical Research: Planets 130, e2024JE008303. https://doi.org/10.1029/2024JE008303

7. ACKNOWLEDGEMENTS

We would like to thank the steering committee for their advice and discussions, and the NOMAD team for their continued operational and scientific support. This work benefitted from the participation in the ISSI team of E. Thiemann and we are thankful for the opportunity for collaboration and discussion. This project acknowledges funding by the Belgian Science Policy Office (BELSPO) with the financial and contractual coordination by the ESA Prodex Office (PEA 4000103401, 4000121493, 4000140753, 4000140863).